ACS OMEGA

Open Access

This article is licensed under CC-BY-NC-ND 4.0

http://pubs.acs.org/journal/acsodf

Article

Electrochemical Study on the Macro-Cell Corrosion of Pipeline Steel Partially Covered by Different Kinds of Mineral Deposits

Limin He, Yihan Wang, Qiliang Zhang, XinCheng Li, Yunze Xu,* and Yi Huang

Cite This: *ACS Omega* 2023, 8, 44013−44029

Read Online

ACCESS | Metrics & More | Article Recommendations

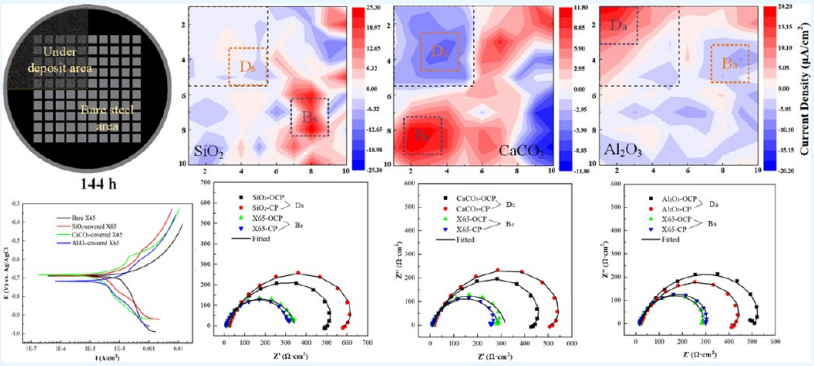

ABSTRACT: This study presents the impact of mineral deposits (SiO_2, Al_2O_3, and $CaCO_3$) on the corrosion behavior of X65 pipeline steel in CO_2-containing brine solution with low pH. The study investigates the initiation and propagation of under deposit corrosion (UDC) using a wire beam electrode (WBE) partially covered by different mineral deposit layers, in conjunction with electrochemical measurements and surface characterization. The results indicate that the corrosion behavior varies, depending on the characteristics of the deposit. During the test period, the Al_2O_3-covered steel acted as the main anode with more negative potential, while the bare steel acted as the cathode. The SiO_2-covered steel acted as the cathode with more positive potential and a localized $FeCO_3$ layer formed beneath the silica mineral. The $CaCO_3$-covered steel initially acted as an anode with a more negative potential but transformed into the cathode at the end of the test. Additionally, shallow and small pits were observed beneath the deposits with the depth in the sequence Al_2O_3 > SiO_2 > $CaCO_3$.

1. INTRODUCTION

The mineral deposits always entrain in the oil and gas production water,[1−4] resulting in the partial coverage of the pipe bottom. The accumulation of the mineral deposits might cause localized corrosion at six o'clock of the pipe circle,[5,6] which is normally defined as under deposit corrosion (UDC).[7,8] Due to the inhibition of the ion diffusion beneath the deposition barrier, the local chemical and electrochemical environment beneath the deposit would be different from that of the steel in the bulk solution.[9,10] Accordingly, the inhomogeneous surface status beneath the deposit[11,12] and the potential difference[13,14] between the bare steel and deposit-covered steel are attributed to the main influencing factors for the initiation and propagation of UDC.

The macro-cell corrosion induced by deposits occurs as a result of the potential difference between the deposit-covered steel and bare steel.[15,16] Once the deposit-covered electrode acted as the anode, the localized corrosion would be more serious along with the increase of the ratio between the bare steel area and the deposit-covered area.[3,17,18] In order to quantify the localized corrosion, Tan et al.[19] first used the wire beam electrode (WBE) technique to monitor the corrosion process of UDC. In this test, the surface of WBE was partially covered by SiO_2 particles to monitor galvanic current and corrosion potential distribution. The results revealed that no localized corrosion occurred under the deposit with a cathodic current in CO_2-saturated solution. However, when WBE was exposed to the atmosphere, the deposit-covered area transferred into anodes with strong anodic current, owing to the difference in dissolved oxygen concentration. It evidently shows that the application of WBE to monitor UDC is satisfactory. Consequently, the WBE technique has been used as an effective method for UDC studies.[4,8,16,20,21]

Received: August 21, 2023
Revised: October 1, 2023
Accepted: October 31, 2023
Published: November 10, 2023

ACS Publications

© 2023 The Authors. Published by American Chemical Society

To restore the mineral deposits presented in oil and gas pipelines, mixed deposits including several species were used in previous studies.[16,20,22] Zhang et al.[20] employed mixed deposits (including sand, clay, corrosion products, and sulfur) to investigate the galvanic corrosion between the deposit-covered electrode and the bare electrode using WBE in CO_2-containing formation water. It was found that the deposit-covered electrode acted as the cathode at 25 °C. However, it transformed into the anode with pitting corrosion at 60 °C, owing to the formation of $FeCO_3$ on the bare electrode. On the other hand, Liu et al.[22] used a partly covered WBE with mixed sand and clay to study UDC in a CO_2-saturated solution at 37 °C. It is observed that the anode tended to occur in the deposit-covered area. It is attributed to the more negative corrosion potential of the steel beneath the deposits in comparison to the bare steel. As a result, it is concluded that various deposits can induce UDC due to different mechanisms. In order to control the UDC that occurred in different cases, the characteristics of the UDC beneath different mineral deposits should be comprehensively studied.

Several researchers have applied some types of deposits on carbon steel to study their behavior.[12,23−25] Jeannin et al.[25] compared silica and clay deposits on the passivity of carbon steel by using cyclic voltammetry in an O_2 environment. The results indicate notable disparities in the corrosion processes beneath the two deposits. It is found that the accumulation of corrosion products led to the cracking of the clay layer, resulting in the loss of its barrier effect. The silica layer could be maintained because the corrosion products tended to grow inside the silica particles and even create a new barrier layer by combining with them. Additionally, Pandarinathan et al.[24] applied three kinds of deposits (SiO_2, $CaCO_3$, and Al_2O_3) to cover a single specimen to study their corrosion behavior using weight loss and electrochemical measurements in a CO_2-containing brine solution. It was found that alumina made the specimen the roughest with the highest corrosion rate, followed by calcite and silica particles. He hypothesizes that this phenomenon is possibly caused by a decrease in pH due to the hydrolysis of alumina. However, Suarez et al.[23] found that the corrosion rate under calcite deposits was the lowest, while those under silica and alumina deposits were close. She believes this was due to the reaction of calcite with carbonate, leading to an increase in the pH on the steel surface. In summary, these findings visualize that the nature of the deposits would influence the interactions between the deposits, steel, and corrosion products. It leads to an inhomogeneous and variable surface status beneath deposits as well as variable corrosion processes. However, the mechanism behind the variation in corrosion caused by different deposits in CO_2-containing solution is still unclear. Moreover, due to the limitations of the electrochemical techniques, the information on localized corrosion and the macro-cell current between the deposit-covered electrode and the bare electrode is also unclear.

As reported in the literature, the oil and gas industries commonly encounter deposits composed of silica sand, calcium carbonate, alumina, corrosion products, organic compounds, etc.[2,3,24] As the major deposits in pipelines, silica sand, calcium carbonate, and alumina might greatly influence the corrosion process of UDC in pipelines. In this work, these three major types of mineral deposits found in pipelines were employed to investigate the macro-cell current between deposit-covered area and bare steel area using the WBE technique in a CO_2-containing solution. To achieve an in-depth insight into the processes associated with UDC, the WBE method was further used in conjunction with electrochemical impedance spectroscopy (EIS) measurement and potentiodynamic polarization (PDP) measurement. Additionally, surface morphology was also characterized and changes in local pH were monitored to get more information on surface status. In the end, the corrosion mechanism caused by these three mineral deposits was discussed.

2. METHODS

2.1. Preparation of the Materials and Test Solution. The material used in this work was API X65 pipeline steel, which was directly cut from subsea pipelines. The main compositions of the steel are (% by weight) C 0.16, Si 0.45, Mn 1.60, P 0.02, S 0.01, V 0.06, Cu 0.20, Ti 0.01, Nb 0.05, and Fe balance. Before tests, the working surfaces of the steel were polished down to 1000 grits of silicon carbide paper. Then, the surfaces of the steel were degreased in alcohol and encapsulated for later use. The test solution employed in this study was a 3.5% NaCl solution (by weight), prepared by combining analytical-reagent-grade sodium chloride with distilled water.

2.2. Mineral Deposits. Three kinds of mineral deposits (SiO_2, $CaCO_3$, and Al_2O_3) of analytical reagent grade were employed in this work. The scanning electron microscopy (SEM) images of these deposits are shown in Figure 1. It is seen

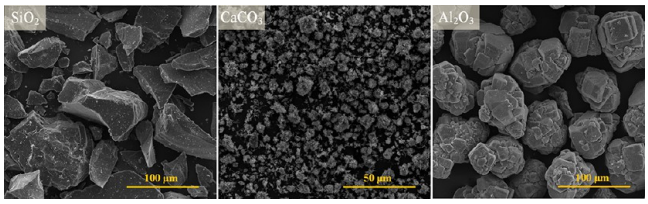

Figure 1. Three different kinds of mineral deposits (SiO_2, $CaCO_3$, and Al_2O_3) used in this work.

that the silica sand particles present irregular shapes with diameters ranging from 5 to 143 μm. The calcite granules present as fine powders with diameters ranging from 1 to 6 μm. The alumina particles present a general round shape ranging from 63 to 94 μm. The general diameters and porosities of the three kinds of mineral deposits are listed in Table 1. It is seen that the porosity of the mineral deposits shows obvious decrease along with the size increase.

Table 1. Properties of the Mineral Deposits

deposits	particle size (μm)	porosity (%)
SiO_2	5−143	40
$CaCO_3$	1−6	80
Al_2O_3	65−94	66

2.3. Test Setup and Procedures. The test setup used for the UDC tests is schematically plotted in Figure 2. The WBE was installed at the bottom of the test cell and sealed by an O ring. The working electrodes (WEs) could be fixed in the test cell through the top cover. A saturated Ag/AgCl electrode and a gauze platinum electrode were employed as the reference electrode (RE) and counter electrode (CE), respectively. The RE and CE were fixed on the top cover, as well. Two pH electrodes (F-71G, Horiba) were inserted into the test cell to measure the local pH changes at both bare steel and deposited areas on WBE. The distance between the tip of the pH electrode

https://doi.org/10.1021/acsomega.3c06189
ACS Omega 2023, 8, 44013−44029

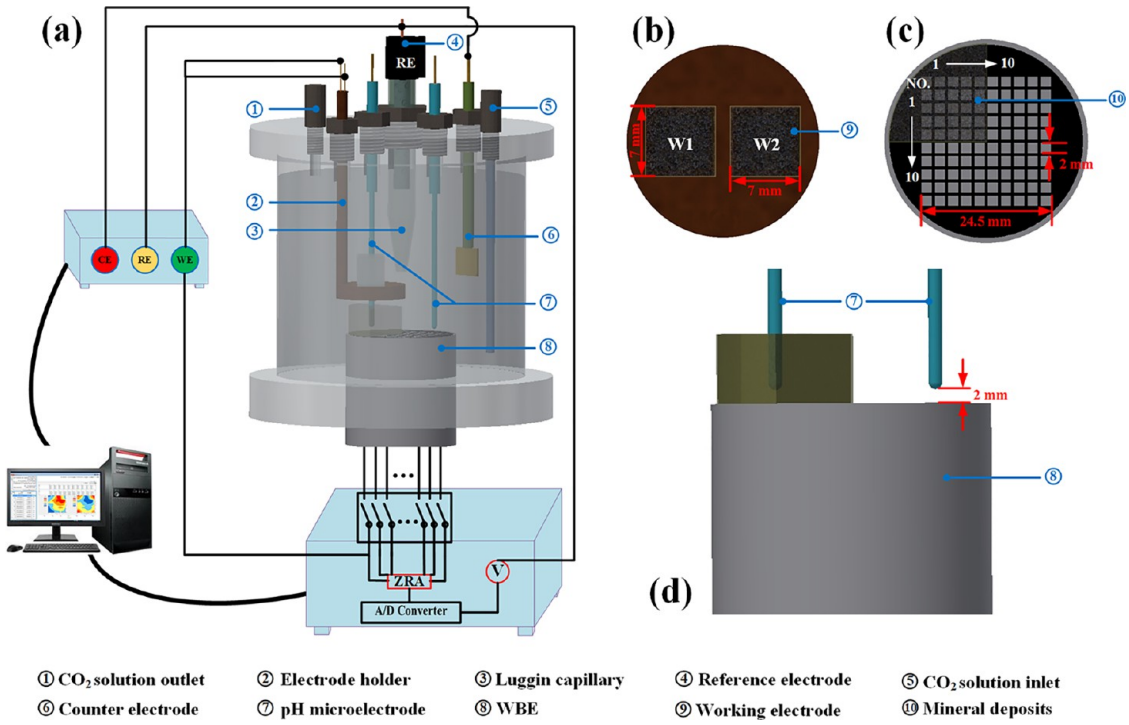

Figure 2. Schematic diagram of the UDC test setup (a), working electrode for the PDP test (b), WBE (c), and pH probe fixed in the test cell (d).

and the WBE surface was 2 mm. The test solution was predeaerated by purging pure CO_2 into the solution for 4 h. Then, the solution was transferred to the test cell using a centrifugal pump. The solution temperature was maintained at 30 ± 1 °C through a water bath, aiming to simulate the oil transfer pipelines operating at the normal temperature in the South China Sea. The CO_2 gas purging was maintained to ensure the CO_2-saturated condition during the test. The pH of the bulk solution in the test cell was maintained at 4 during the test.

A 10 × 10 WBE (Figure 2) made of X65 steel was adopted to probe the macro-cell corrosion induced by the local covering of the mineral deposits. The surface area of the wire electrodes was 2 × 2 mm^2 and the interval of the wire electrodes was 0.5 mm. A square plastic groove was placed in the top left corner of the WBE, covering 5 rows and 5 columns, allowing for the addition of mineral deposits up to a depth of 10 mm. The ratio of the bare steel area and deposit covered area was 3:1, which simulates the normal UDC conditions in real pipelines.[3,12] The measurement principle of the WBE has been introduced in previous studies.[8] Both the open circuit potential (OCP) and macro-cell current distributions on the WBE were mapped by the electrochemical instrument (YC-2200A, YunChi), which consists of a high voltage meter, multichannel zero resistance ammeters (ZRA) and a multiplexer. Generally, the 100-wire electrodes were electrically connected to simulate a one-piece electrode. During the potential mapping, the wire electrodes were disconnected from the other wire electrodes in sequence. The macro-cell current flowing in or out of a single wire electrode could be measured by connecting the ZRA between the selected electrode and the rest electrodes.

Three groups of tests were conducted in this work by adding different kinds of mineral deposits (SiO_2, $CaCO_3$, and Al_2O_3) to the test cell. Each set of tests lasted for a duration of 6 days. During the test, the potential and current mapping were conducted every 1 h to identify the local anodic and cathodic sites on the steel surface. Some typical areas that were located beneath the deposits and at the bare steel area were selected for local EIS measurements at different test periods. During the EIS measurement, the selected wire electrodes were connected to the electrochemical workstation (Figure 2) through the multiplexer. In order to investigate the macro-cell effect on the corrosion behavior of pipeline steel beneath deposits, the EIS measurements were carried out at both the OCP and the coupled potential. The coupled potential indicates the potential of the whole WBE when the 100-wire electrodes are all electrically connected. Prior to the EIS measurements, the coupled potential of the steel surface was determined. The EIS measurement frequency ranged from 10^5 Hz to 0.01 Hz with a sinusoidal amplitude of 10 mV.

After the three groups of WBE tests, the deposits and porous rust on the surface of WBE were first washed with deionized water. Then, the surfaces of the wire electrodes were observed with a laser scanning confocal microscope (LEXT OLS5000, Olympus). The compositions of the corrosion products on the WBE were analyzed by Raman Spectroscopy (DXR microscope, Thermo Fisher). Thereafter, the corrosion products on the WBE were cleaned by the acid pickling suggested in ASTM G1-03. The 3D profile of the WBE was further examined by a laser scanning confocal microscope.

The potentiodynamic polarization (PDP) measurements were performed on the steel electrodes to understand the influences of mineral deposits on the cathodic and anodic reactions.[24,26] The WEs were machined in the size of 7 × 7 mm^2, as shown in Figure 2. Four groups of PDP measurements were conducted to obtain the polarization curves of the steel covered by different kinds of mineral deposits (bare steel and steel covered by SiO_2, $CaCO_3$, and Al_2O_3, respectively). In each group of tests, two parallel steel electrodes were used to obtain the polarization curves at the beginning of the test and at the end of the test. The WE1 was used after 2 h of immersion and WE2 was used after 144 h of immersion. The thickness of the deposit

https://doi.org/10.1021/acsomega.3c06189
ACS Omega 2023, 8, 44013−44029

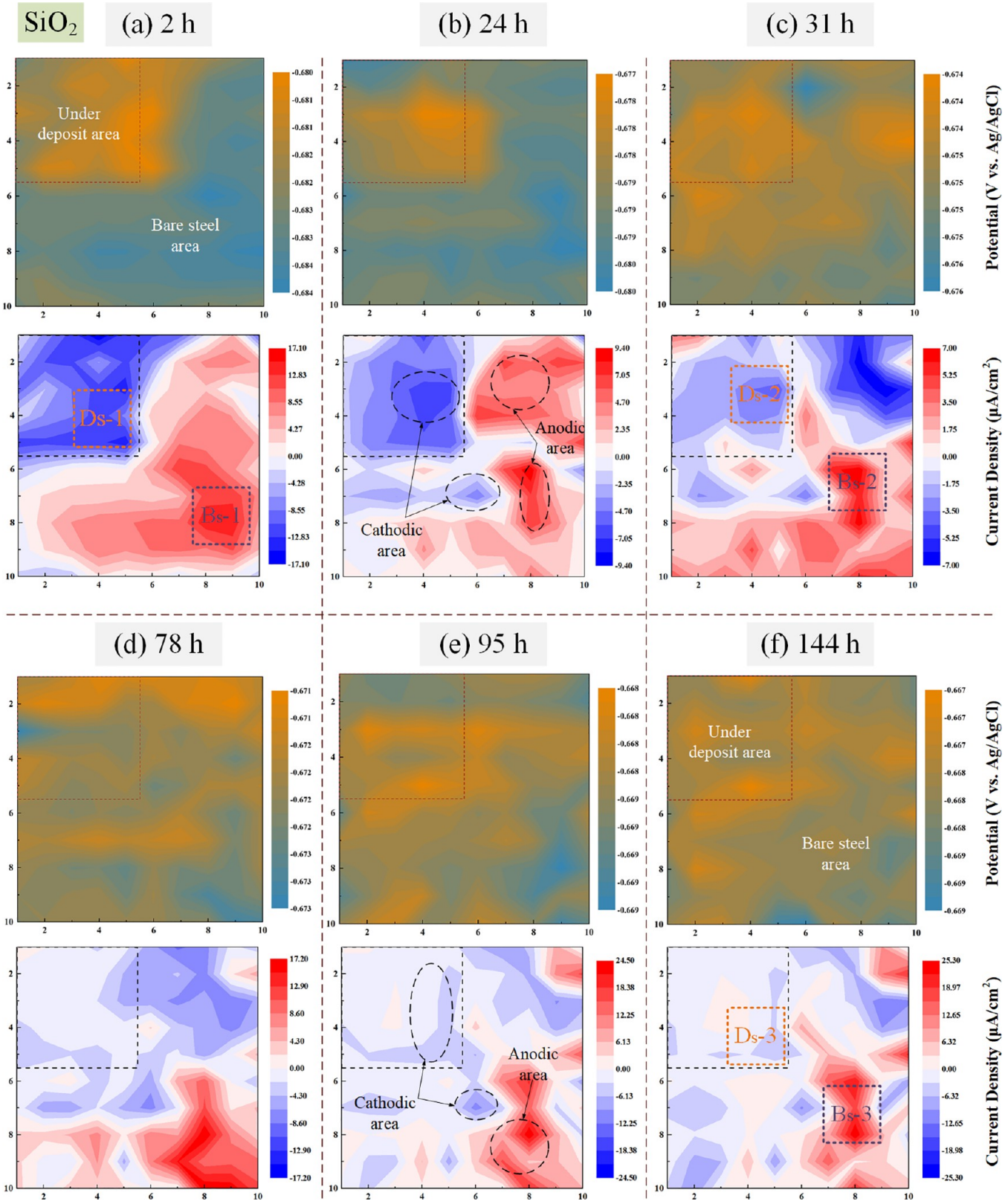

Figure 3. Distributions of the potential and macro-cell current on the SiO_2-covered WBE at different test periods: (a) 2 h, (b) 24 h, (c) 31 h, (d) 78 h, (e) 95 h, and (f) 144 h.

layer was also 10 mm. The PDP measurements were conducted by anodically polarizing the steel from −0.3 to + 0.3 V (vs OCP) with a scan rate of 0.5 mV/s.

Both the WBE and PDP tests were repeated twice to ensure repeatability. Furthermore, an additional immersion test (similar to the WBE test) was conducted to obtain more surface information about the corrosion products. After the immersion

https://doi.org/10.1021/acsomega.3c06189
ACS Omega 2023, 8, 44013−44029

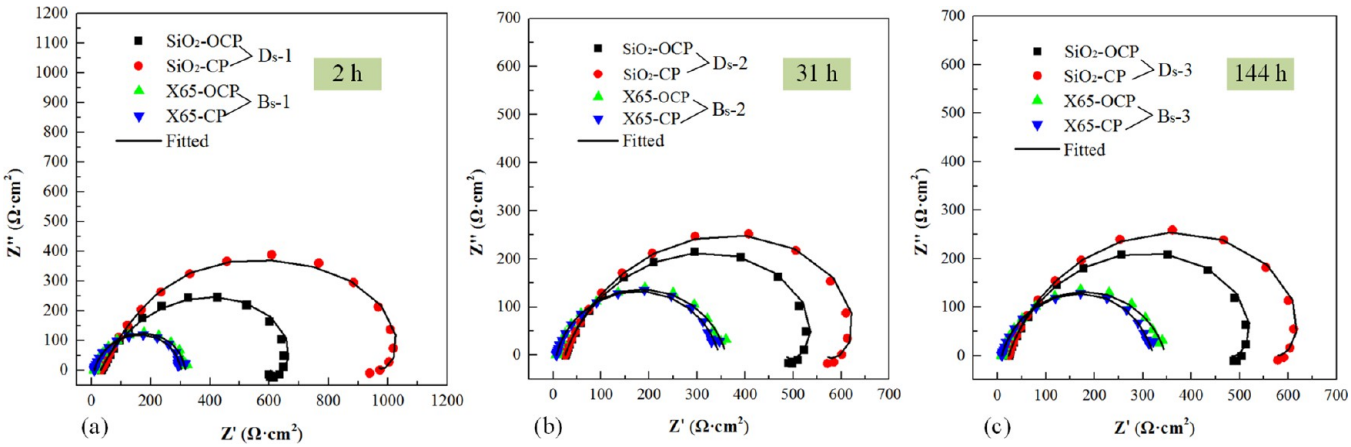

Figure 4. EIS and fitted curves of the bare steel electrode and the electrodes covered by SiO_2 at different periods: (a) 2 h, (b) 31 h, and (c) 144 h.

test, the morphology of the steel coupon beneath deposits was observed using scanning electron microscopy (SEM, EM-20AX Plus, Coxem), and the corrosion products were identified by X-ray diffraction (XRD) using an EMPYREAN (PANalytical, Holland) instrument in the 2θ ranging from 20° to 80° with a Cu Kα source.

3. RESULTS

3.1. UDC Performance under SiO_2 Deposit Using WBE. Figure 3 shows the distribution maps of potential and macro-cell current at different test periods when the top-left quarter of the WBE was covered by the SiO_2 deposit. It is seen from Figure 3a,b that the main cathodic sites were located at the deposit-covered area on the first day of immersion. The bare steel areas all acted as anodic sites. After 31 h of immersion, as shown in Figure 3c,d, although most of the deposit-covered area acted as the cathodes, the highest cathodic current was found on the wire electrodes outside the deposit-covered area. Both the anodic currents and cathodic currents show an obvious decrease along with the corrosion propagation (Figure 3e,f). Some small anodic sites where tiny anodic currents were registered appeared in the center of the deposit-covered area. When the steel was partially covered by SiO_2 deposit, the highest potential difference was only 4 mV and the highest anodic current was −17.1 μA/cm^2, indicating a relatively uniform corrosion on the WBE. The covering of the SiO_2 would not induce obvious UDC under the employed test condition.

Based on the WBE measurements, several typical areas that exhibit significant anodic or cathodic currents were selected for further investigation through EIS measurements. The selected cathodic areas (Ds 1−3) beneath the deposit and the selected major anodic areas (Bs 1−3) on the bare steel surface are marked in Figure 3. The EIS performances of these typical areas at different test periods (2, 31, and 144 h) are plotted in Figure 4. The capacitive semicircles of both the deposit-covered area and the bare steel area are observed, indicating that the corrosion is under charge transfer control.[27] It is seen that the impedance of the deposit-covered area was much larger than that of the bare steel at the OCP. The diameter of the semicircle showed an obvious increase when the deposit-covered steel was working at coupled potentials (−683, −675, and −668 mV), indicating that the macro-cell current would inhibit the corrosion beneath the deposit. No obvious changes in the EIS performance were observed for the bare steels at coupled potentials.

In addition, a small inductive semicircle is observed in the low-frequency range at the SiO_2-covered area. It might be induced by the adsorption of $FeOH_{ads}$ beneath the deposit.[28] As a result, the equivalent circuits shown in Figure 5a,b are used to fit the EIS

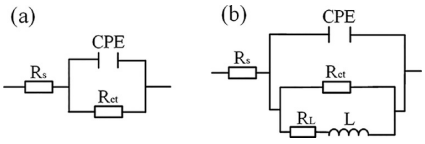

Figure 5. Equivalent circuit used for fitting the EIS results: bare steel area (a) and deposit-covered area (b).

results of the bare steel area and deposit-covered area, respectively.[28] The fitted results are listed in Table 2, where R_{ct} is the charge transfer resistance, R_L is the inductive resistance, L is the inductance, and CPE is the constant phase element representing the capacitance of the double layer. The CPE impedance (Z_{CPE}) can be described as:[29]

$$Z_{CPE} = 1/(Qj\omega)^n \quad (1)$$

where Q is a proportional factor (CPE), and n is the CPE exponent. The element CPE behaves as a pure capacitance when n is 1 and a pure resistance when n is 0. It is seen that the R_{ct} of the deposit-covered area decreased as the immersion time increased. The R_{ct} of the bare steel area increased slightly along the corrosion propagation. The n value of the steel beneath the deposit is lower than that of the bare steel, indicating a more inhomogeneous surface status at the deposit-covered area.

3.2. UDC Performance under $CaCO_3$ Deposit Using WBE. Figure 6 shows the potential and macro-cell current maps of the WBE covered by the $CaCO_3$ deposit. It can be visualized from Figure 6a,b that, contrary to the SiO_2 particles, the electrodes beneath the $CaCO_3$ powder served as the primary anodes during the initial 24 h of the experiment. After that, it is seen from Figure 6c,d that the anodic current and anodic sites beneath the deposit show an obvious decrease along with the test. Correspondingly, the cathodic current and cathodic sites beneath the deposit increased gradually until the electrodes completely transformed into the cathode after 72 h immersion, and this state remained until the end of the experiment (Figure 6e,f). Figure 6 shows that when the steel is partially covered by $CaCO_3$ powder, the highest potential difference was 17 mV and the highest anodic current was 22.2 μA/cm^2 initially. However, the potential difference decreased to 2 mV and the anodic

https://doi.org/10.1021/acsomega.3c06189
ACS Omega 2023, 8, 44013−44029

Table 2. Fitted Results of the Electrode with and without SiO_2

		R_s (Ω cm^2)	$Q \times 10^{-4}$ (Ω^{-1} cm^{-2} s^{-n})	n	R_{ct}(Ω cm^2)	L (H cm^{-2})	R_L(Ω cm^2)
2 h	SiO_2-OCP	32.81	4.59	0.73	786	4409	2187
	SiO_2-CP	32.19	4.61	0.74	1101	6280	2356
	X65-OCP	10.49	5.43	0.84	311.8		
	X65-CP	10.45	5.4	0.84	297		
31 h	SiO_2-OCP	27.05	8.79	0.79	609.7	7075	1933
	SiO_2-CP	27.09	8.82	0.78	716.7	10130	2328
	X65-OCP	10.28	7.7	0.84	351. 9		
	X65-CP	10.27	7.71	0.84	338.5		
144 h	SiO_2-OCP	25.81	10.06	0.8	592.6	7952	2116
	SiO_2-CP	25.96	10.12	0.79	713.3	11670	2562
	X65-OCP	10.21	10.81	0.84	338.4		
	X65-CP	10.17	10.92	0.85	316.6		

current decreased to around −6.5 μA/cm^2 after 65 h of immersion. It might be due to the adsorption of $CaCO_3$ on the carbon steel surface, preventing aggressive ions from reaching the steel surface. The results indicate that the covering of the $CaCO_3$ would not induce obvious UDC under the employed test condition.

Similar to the case for SiO_2 particles, the typical areas selected for EIS measurements are marked in Figure 6. The areas beneath the deposit were labeled as Dc 1-3, while the areas on the bare steel surface were labeled as Bc 1-3. Based on the results of WBE, the EIS performances of these typical areas were selected at 2, 48, and 144 h and are plotted in Figure 7. The presence of capacitive and inductive semicircles in both the deposit-covered and bare steel areas is similar to that of SiO_2 particles, which indicates that charge transfer controls the corrosion process. The deposit-covered area exhibited significantly higher impedance than the bare steel area at OCP. The diameter of the semicircle noticeably decreased, when the deposit-covered steel was operated at coupled potentials (−686 mV) after the initial 2 h of immersion, indicating that the macro-cell current aggravated corrosion beneath the deposit. During the test, the impedance of the electrodes beneath the $CaCO_3$ powder at the coupled potential (−683 and −678 mV) constantly approached and eventually surpassed that of the OCP, suggesting that the macro-cell current significantly inhibited iron dissolution of the $CaCO_3$-covered electrode. The EIS performance of the bare steels at coupled potentials was consistent with that of the deposit-covered area. However, the observed changes do not appear to be particularly significant overall.

Same as the SiO_2 particles, the equivalent circuits presented in Figure 5a,b were used to model the EIS results of the bare steel area and the $CaCO_3$-covered area, respectively. The fitted parameters are given in Table 3. As the immersion time increased, the R_{ct} of the deposit-covered electrode decreased, while that of the bare electrode showed a slight increase. Additionally, the n value was lower for the steel beneath deposits compared to the bare steel, implying a less homogeneous surface status in the deposit-covered area.

3.3. UDC Performance under Al_2O_3 Deposit Using WBE. Figure 8 illustrates that the main anodic sites were located in the deposit-covered area during this test. It is seen from Figure 8a,b that the main anodic sites were concentrated in the bottom-right region of the deposit. Then, the anode area shifted and was concentrated in the top-left region of the deposit, as shown in Figure 8c−f. When the steel was partially covered by the Al_2O_3 deposit, the highest potential difference between the deposit-covered area and the bare steel area was 13 mV, gradually stabilizing at about 5 mV. The highest anodic current density was 44.40 μA/cm^2, gradually reducing to around 20 μA/cm^2 (0.23 mm/y). It indicates that corrosion under a deposit on the WBE was exacerbated, and the Al_2O_3 deposit contributed to sharpening the UDC under this test condition.

The typical regions of WBE chosen for EIS measurements in this work are marked in Figure 8, the areas beneath the deposit marked as Da 1-3, and the areas on the bare steel marked as Ba 1-3. Based on the results of WBE, the EIS results of these areas at different test periods (2, 66, and 144 h) are displayed in Figure 9. It is seen that the corrosion is controlled by charge transfer, supported by the capacitive semicircles in the deposit-covered and bare steel areas, similar to the case for SiO_2 particles and $CaCO_3$ powder. It is also seen that the deposit-covered area displayed a significantly higher impedance compared to the bare steel area at OCP. The semicircle diameter significantly reduced when the deposit-covered steel worked at coupled potentials (−679, −678, and −678 mV), especially when the WBE was soaked for 2 h. This suggests that corrosion beneath the deposit was accelerated by the macro-cell current. Correspondingly, a slight increase in the diameters of the semicircles is observed for the bare steels at coupled potentials. Additionally, a similar small inductive semicircle is observed in the Al_2O_3-covered area at a low-frequency range.

The EIS data were fitted with the equivalent circuits in Figure 5, and the fitted results are presented in Table 4. It is seen that, during the test, the R_{ct} of the deposit-covered electrode shows an obvious reduction, while the R_{ct} of the bare electrode shows a negligible increase. The n value of the steel beneath the deposit increased but remained lower than that of the bare steel. It suggests that the surface of the area covered by deposits is less homogeneous.

The current of every electrode beneath the deposit was added as the macro-cell current between the deposit-covered area and the bare steel area. Figure 10 shows the variation of current density over time with a 6 h interval. It is seen that the area covered by SiO_2 particles was monitored as a cathode, indicating that the corrosion under SiO_2 particles was inhibited. It is also seen that the $CaCO_3$-covered area acted as an anode initially. However, the anodic current decreased gradually and turned to the cathodic current, since the WBE was immersed for about 60 h. Hereafter, the cathodic current stabilized at about −4.8 μA/cm^2, larger than the current (−1.7 μA/cm^2) monitored in the test covered by SiO_2 particles. Thus, the corrosion under $CaCO_3$ powder was also inhibited in this test condition. On the other hand, the Al_2O_3-covered area acted as an anode during the test. The anodic current was largest at the beginning of the test and

https://doi.org/10.1021/acsomega.3c06189
ACS Omega 2023, 8, 44013−44029

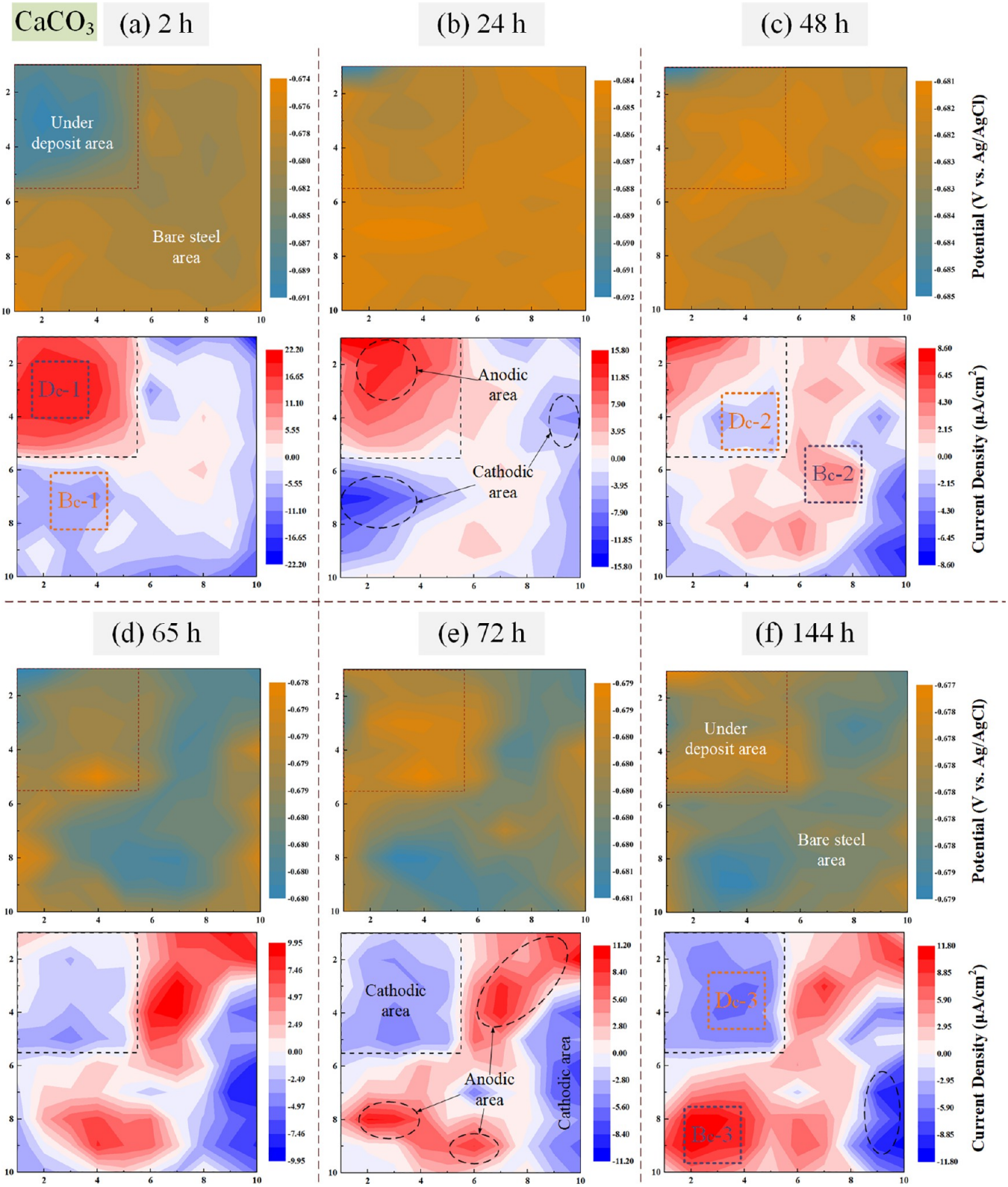

Figure 6. Distributions of the potential and macro-cell current on the $CaCO_3$-covered WBE at different test periods: (a) 2 h, (b) 24 h, (c) 48 h, (d) 65 h, (e) 72 h, and (f) 144 h.

gradually stabilized at around 6.7 $\mu A/cm^2$, which was approximately one-third of the maximum current plotted in Figure 8. It indicates that the macro-cell current between the deposit-covered area and bare steel area exacerbated the corrosion under Al_2O_3 particles; however, it was not sufficiently sensitive to detect localized corrosion.

3.4. Potentiodynamic Polarization Measurement. Figure 11 shows the results of the potentiodynamic polarization measurement conducted on the bare steel samples and the

https://doi.org/10.1021/acsomega.3c06189
ACS Omega 2023, 8, 44013−44029

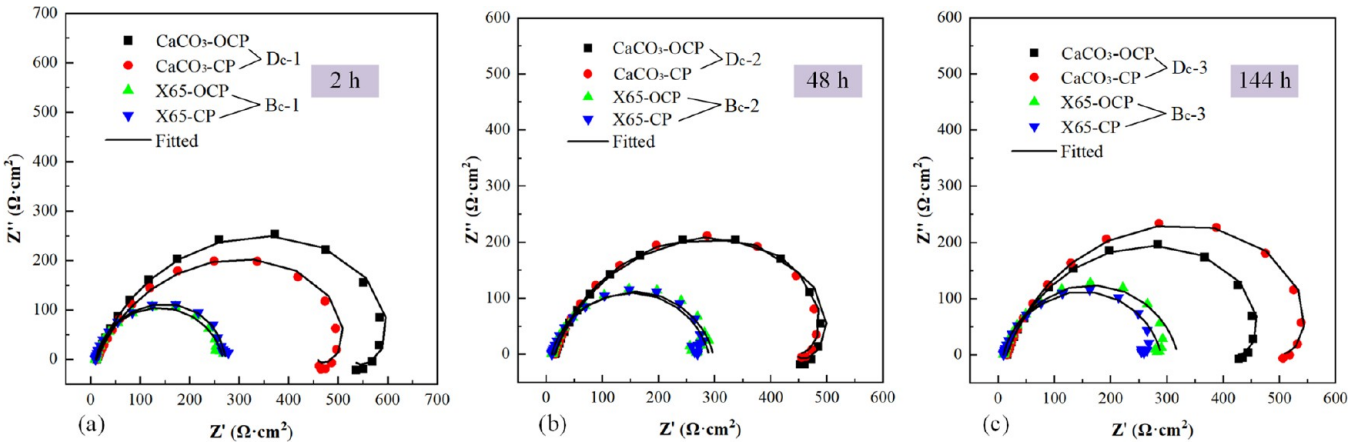

Figure 7. EIS and fitted curves of bare steel electrode and the electrodes covered by $CaCO_3$ at different periods: (a) 2 h, (b) 48 h, and (c) 144 h.

Table 3. Fitted Results of the Electrode with and without $CaCO_3$

		R_s (Ω cm^2)	$Q \times 10^{-4}$ (Ω^{-1} cm^{-2} s^{-n})	n	R_{ct} (Ω cm^2)	L (H cm^{-2})	R_L(Ω cm^2)
2 h	$CaCO_3$-OCP	13.12	10.56	0.79	712.8	7753	1808
	$CaCO_3$-CP	14.43	7.56	0.75	621.9	4083	1650
	X65-OCP	9.79	11.71	0.87	268		
	X65-CP	9.75	11.72	0.87	278.4		
48 h	$CaCO_3$-OCP	14.98	10.52	0.79	586	6365	1672
	$CaCO_3$-CP	14.27	12.82	0.80	587.4	6566	1809
	X65-OCP	10.37	6.81	0.85	310.8		
	X65-CP	10.40	6.83	0.85	308.4		
144 h	$CaCO_3$-OCP	15.65	12.95	0.80	547.6	6173	1705
	$CaCO_3$-CP	15.69	12.89	0.80	656.3	8841	2033
	X65-OCP	10.16	15.95	0.86	315.5		
	X65-CP	10.18	15.82	0.86	291.1		

deposit-covered samples after exposure to the test solution for 2 and 144 h. It is seen that the presence of deposits causes differential decreases in the anodic and cathodic current densities at the same polarized potential. In the first 2 h of the test, there was a positive shift in the corrosion potential for the SiO_2-covered sample compared with the bare steel sample. The corrosion potential for the $CaCO_3$ and Al_2O_3-covered samples experienced a negative shift. Therefore, when coupled to the bare steel sample, the SiO_2-covered electrode would act as the cathode while the $CaCO_3$ and Al_2O_3-covered electrodes would behave as anodes. After immersion for 144 h, there was still a positive shift and a negative shift for the SiO_2-covered electrode and the Al_2O_3-covered electrode compared with bare steel samples, respectively. However, the corrosion potential of the $CaCO_3$-covered electrode moved positively and surpassed that of the bare steel electrode. Additionally, a transition similar to the passivation process occurred in the anodic region of the $CaCO_3$-covered electrode, which might be related to the anode and cathode transition shown in Figure 6.

It is seen from Figure 11 that both the cathodic and the anodic current densities decreased significantly under the same overpotential, suggesting that both the cathodic and anodic reactions were suppressed. Additionally, multiple polarization branches are observed in the polarization curve, particularly in the cathodic region of deposit-covered electrodes. This may be attributed to the blocking effect of deposits on the ion diffusion. During the measurements, there was a constant depletion of H^+ as the polarization potential moved toward the corrosion potential. As a result, the cathodic reaction changed from mixed control to diffusion control.[20,30] Similarly, the obstruction of ion diffusion by deposits also affected the anodic polarization process.

Polarization curves provide valuable insights into the mechanism of iron dissolution through analysis of the Tafel slope changes.[31−33] It is well known that the anodic and cathodic slopes are determined by the Tafel extrapolation method.[23] In the strong polarization region of the cathodic branch, there are observable long linear sections that could be used to fit the cathodic Tafel slope. However, the anodic branch does not show wide Tafel linear behavior. The value of b_a increased as the anodic potential shifted positively. To obtain a more accurate corrosion rate (CR), the anodic region between 80 and 120 mV vs OCP (the strong anodic polarization region) was selected to determine the anodic Tafel slope.[29,34,35] The fitted results derived from the polarization curves are given in Table 5. It is observed that b_a for the bare steel was close to 60 mV, while the electrodes covered by the deposits show even higher b_a values. It could be attributed to the blocking effect of cations diffusion caused by the presence of deposits on the electrode surface. It is also seen that the anodic and cathodic slopes show a relatively slight variation during the test, indicating that the corrosion processes may be unchanged. The *CR* of the deposit-covered electrode shows a slight increase, while the *CR* of the bare steel electrode shows no obvious changes. The corrosion rates derived from the polarization curves are consistent with those of the EIS results. It is also seen that the corrosion potential of the $CaCO_3$-covered electrode shifted in a positive direction by 34 mV during the test.

https://doi.org/10.1021/acsomega.3c06189
ACS Omega 2023, 8, 44013−44029

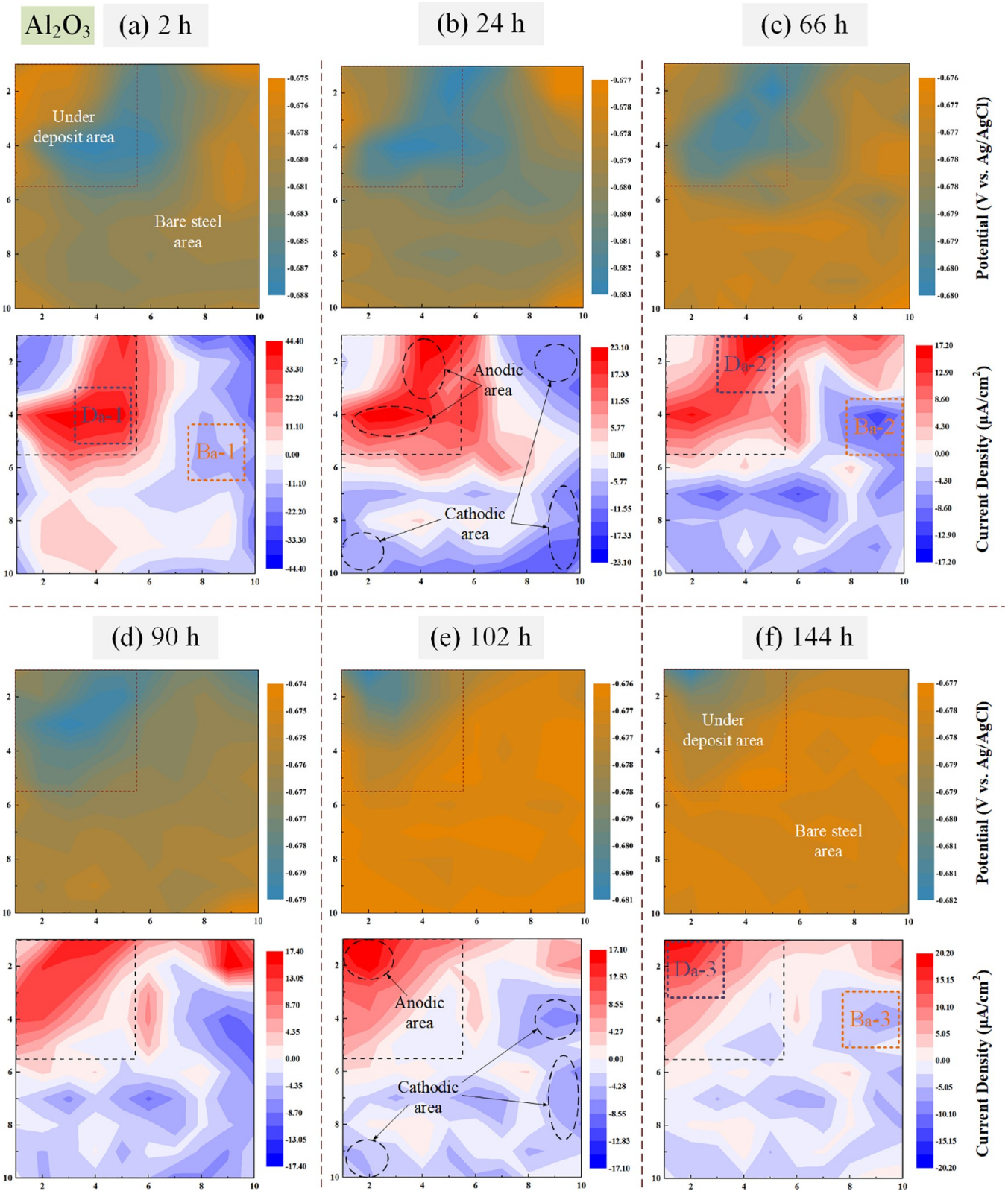

Figure 8. Distributions of the potential and macro-cell current on the Al_2O_3-covered WBE at different test periods: (a) 2 h, (b) 24 h, (c) 66 h, (d) 90 h, (e) 102 h, and (f) 144 h.

3.5. Characterization of the Surface Morphology and Deposits. Figure 12 shows the representative surface morphologies of the deposit-covered area after the WBE was immersed for 144 h. It is seen that a localized corrosion product layer was found on the steel surface beneath the SiO_2 deposit, which was demonstrated as $FeCO_3$ by Raman,[36] as shown in Figure 13. Meanwhile, some scattered $FeCO_3$ crystals were observed on the steel surface beneath Al_2O_3, as shown in Figures 12c and 13. However, these crystals could be easily brushed off by a soft brush. It is also seen from Figure 12b that a layer

https://doi.org/10.1021/acsomega.3c06189
ACS Omega 2023, 8, 44013−44029

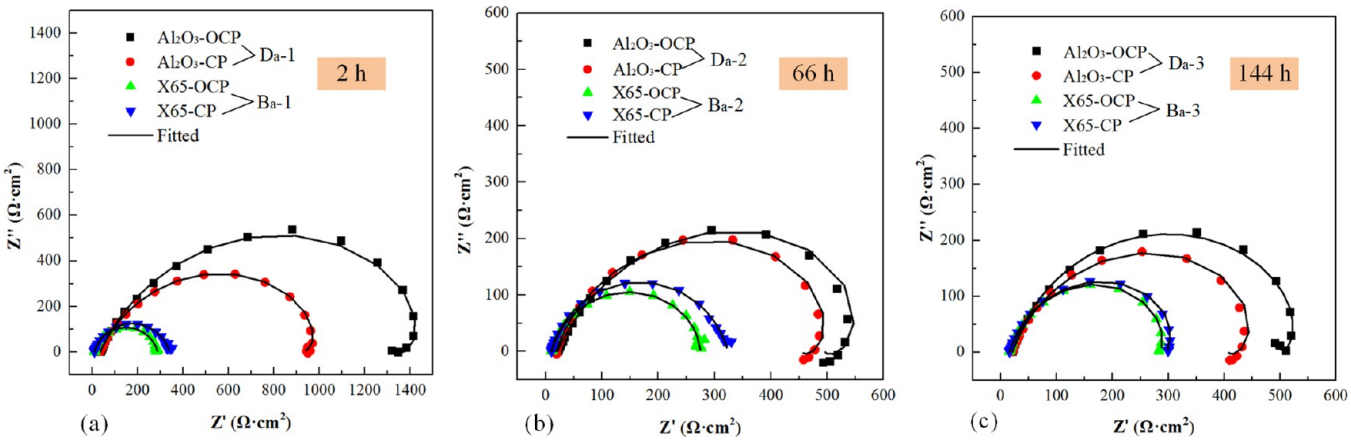

Figure 9. EIS and fitted curves of the bare steel electrode and the electrodes covered by Al_2O_3 at different periods: (a) 2 h, (b) 31 h, and (c) 144 h.

Table 4. Fitted Results of the Electrode with and without Al_2O_3

		R_s (Ω cm^2)	$Q \times 10^{-4}$ (Ω^{-1} cm^{-2} s^{-n})	n	R_{ct} (Ω cm^2)	L (H cm^{-2})	R_L (Ω cm^2)
2 h	Al_2O_3-OCP	25.66	2.72	0.73	1607	31790	7389
	Al_2O_3-CP	25.84	2.67	0.73	1069	15460	6284
	X65-OCP	10.48	4.57	0.83	278.1		
	X65-CP	10.48	4.79	0.82	330.3		
66 h	Al_2O_3-OCP	17.97	9.62	0.74	580.5	5389	1649
	Al_2O_3-CP	17.62	11.36	0.78	466.9	4585	1458
	X65-OCP	10.44	4.47	0.84	268.2		
	X65-CP	10.2	7.32	0.84	313.1		
144 h	Al_2O_3-OCP	16.18	10.43	0.78	561.2	8986	2032
	Al_2O_3-CP	16.77	9.91	0.81	516.2	10032	2000
	X65-OCP	11.09	13.59	0.85	283		
	X65-CP	11.14	13.78	0.85	300		

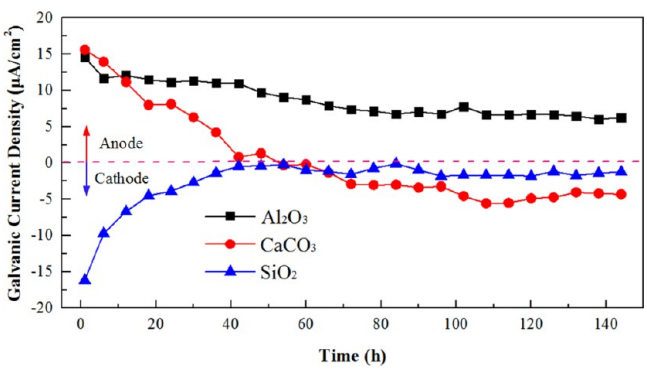

Figure 10. Galvanic current density between the bare steel area and the deposit-covered area of the WBE.

adheres to the steel surface, and it was detected by Raman with a result of $CaCO_3$ and slight $Fe_xCa_{1-x}CO_3$,[37,38] as shown in Figure 13. In addition, the morphologies of coupon steel in the appendix immersion test coincided with the WBE test, and the composition of corrosion products identified by XRD in the appendix immersion test was consistent with those of the Raman test, as shown in Figures A1 and A2 of the Appendix. Figure A1 clearly shows the presence of gaps on the localized $FeCO_3$ layer, leading to direct exposure of the carbon steel to the solution. The gaps between the $FeCO_3$ crystals contribute to the formation of pits.

After the removal of the corrosion product, slight pitting was found beneath the deposits. The pitting depth was in sequence Al_2O_3 > SiO_2 > $CaCO_3$, as shown in Figure 12. It is seen from Figure 8 that the main anodic current occurred beneath the Al_2O_3 deposit during the test, which led to increased iron dissolution of the deposit-covered steel. It suggests that Al_2O_3 particles could lead to more serious localized corrosion in the CO_2-containing pipelines. Though the anodic current was initially located in the $CaCO_3$-covered area, its distribution was uniform, as shown in Figure 6. Additionally, the anodic current transformed to a uniform cathodic current after 65 h. Therefore, the corrosion of the area covered by $CaCO_3$ powder tended to show a more uniform behavior. However, the cathodic current beneath the SiO_2 deposit was nonuniform and accompanied by tiny anodic currents due to the lower porosity of the SiO_2 particles, as shown in Figure 3. Moreover, a localized $FeCO_3$ layer with gaps was observed on the SiO_2-covered area, as shown in Figure 12 and Figure A1 of the Appendix. These contributed to the localized corrosion, resulting in the formation of pits with the minimum diameter.

Figure 14 presents the local pH variation on both the deposit-covered electrode and its coupled bare steel electrode (solution, pH 4). It is seen from Figure 14a that the pH beneath the SiO_2 particles is around 6.3 and higher than that of the bare steel. Figure 14b,c shows that the pH values beneath the $CaCO_3$ powder and Al_2O_3 particles could reach 6.8 and 7.9 in the initial test, respectively. This can be attributed to the active nature of Al_2O_3 and $CaCO_3$ in the brine solution containing CO_2. It is reported the pH of $CaCO_3$ is approximately 9.9,[23] which was much higher than the bulk solution. Furthermore, the $CaCO_3$ on the steel surface could undergo hydrolysis into Ca^{2+} and HCO_3^- in the solution containing CO_2 by the following reaction[23]:

https://doi.org/10.1021/acsomega.3c06189
ACS Omega 2023, 8, 44013−44029

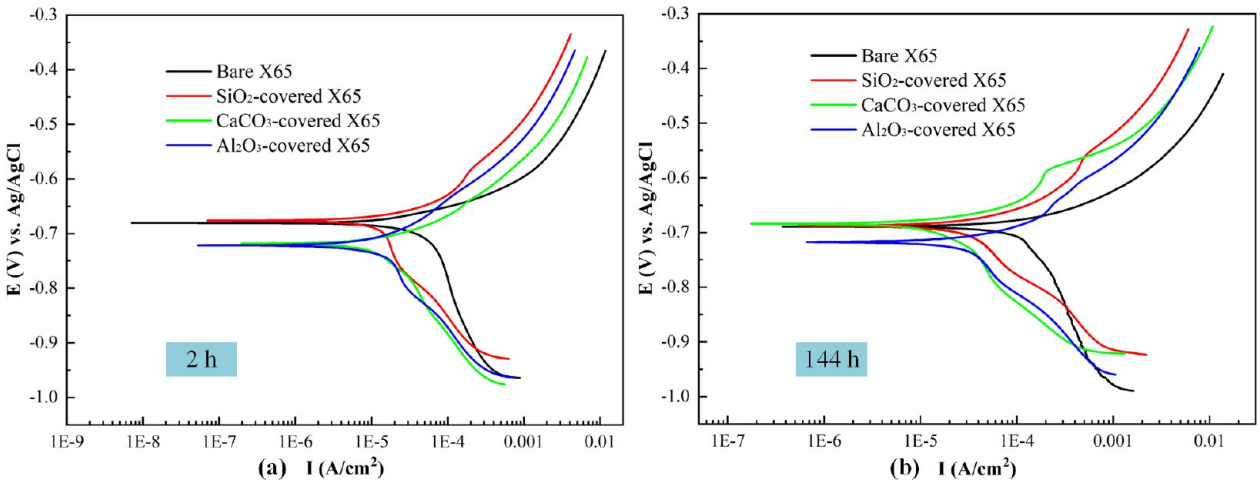

Figure 11. PDP of the bare steel electrode and the electrodes covered with different minerals at 2 h (a) and 144 h (b).

Table 5. Parameters from the Polarization Curves

time	deposit	b_a (mV/dec)	$-b_c$ (mV/dec)	E_{corr} ($V_{Ag/AgCl}$)	i_{corr} ($\mu A/cm^2$)	CR (mm/y)
2 h	SiO_2	101.8	220.1	−0.681	30.7	0.36
	$CaCO_3$	82.8	184.6	−0.718	27.3	0.32
	Al_2O_3	106.5	178	−0.721	17.4	0.20
	bare	57.2	480.9	−0.685	63.7	0.75
144 h	SiO_2	103.6	224.2	−0.687	37.3	0.44
	$CaCO_3$	73.4	140.3	−0.684	29.4	0.34
	Al_2O_3	85.5	187.6	−0.717	31.8	0.37
	bare	59.5	420.8	−0.689	61.9	0.72

$$CaCO_3 + H_2O + CO_2 \rightarrow Ca(HCO_3)_2 \rightarrow Ca^{2+} + 2HCO_3^- \quad (2)$$

Bicarbonate ions in the solution could suppress the ionization of carbonic acid, leading to an increase in the pH on the $CaCO_3$-covered steel surface. As for Al_2O_3, its property in solution is different from $CaCO_3$. Al_2O_3 could hydrolyze in the solution into $Al(OH)_3$, it also could react with H^+ in a low pH solution (pH < 4).[39,40] Following the immersion test described in the Appendix, partial dissolution of Al_2O_3 particles was observed, as shown in Figure A1. Additionally, the measurement results indicate a higher pH below that of the Al_2O_3 particles. Therefore, the following reaction might occur in the test brine solution containing CO_2:

$$Al_2O_3 + 6H^+ \rightarrow 2Al^{3+} + 3H_2O \quad (3)$$

Along with the WBE immersion, the pH of the deposit-covered steel tended to stabilize and was relatively close (Figure 14d), falling between 6.1 and 6.6, which was about 0.6 units higher than that of bare steel.

4. DISCUSSION

During the corrosion test in a brine solution containing CO_2, anodic corrosion involves many steps. The multistep dissolution of carbon steel could proceed in the following anodic reactions[33,41,42]:

$$Fe + H_2O \rightarrow FeOH_{ads} + H^+ + e^- \quad (4)$$

$$FeOH_{ads} \rightarrow FeOH^+ + e^- \quad (5)$$

$$FeOH^+ + H^+ \rightarrow Fe^{2+} + H_2O \quad (6)$$

The inductive semicircle presented in the low frequency of the EIS results was related to the coverage of adsorbed intermediate product $FeOH_{ads}$ on the surface.[30] However, there was only one capacitive semicircle on the bare steel surface. It might be attributed to the large corrosion rate on the bare steel surface, leading to the accumulation of the $FeOH_{ads}$ on the electrode surface.[41,43]

The cathodic reaction only considered is hydrogen evolution reaction on the bare steel in this test (solution pH 4).[44,45] In addition, the water reduction process would appear below −0.9 V,[30] which could dominate the cathodic polarization curves as shown in Figure 11. The cathodic reactions could be summarized by the following equations[33,44,45]

$$2H^+ + 2e^- \rightarrow H_2 \quad (7)$$

$$2H_2O + 2e^- \rightarrow 2OH^- + H_2 \quad (8)$$

Based on the pH measurements, it was observed that the pH was higher beneath the deposits. Therefore, it is possible that carbonic acid and bicarbonate ions also play a role in the cathodic reaction as follows[28,42]:

$$2H_2CO_3 + 2e^- \rightarrow 2HCO_3^- + H_2 \quad (9)$$

$$2HCO_3^- + 2e^- \rightarrow 2CO_3^{2-} + H_2 \quad (10)$$

During the corrosion process, the concentrations of Fe^{2+} and CO_3^{2-} will increase gradually until reaching the solubility product of $FeCO_3$ on the carbon steel surface.[46] Thus, the $FeCO_3$ corrosion scale may form through precipitation reactions as the following:

https://doi.org/10.1021/acsomega.3c06189
ACS Omega 2023, 8, 44013−44029

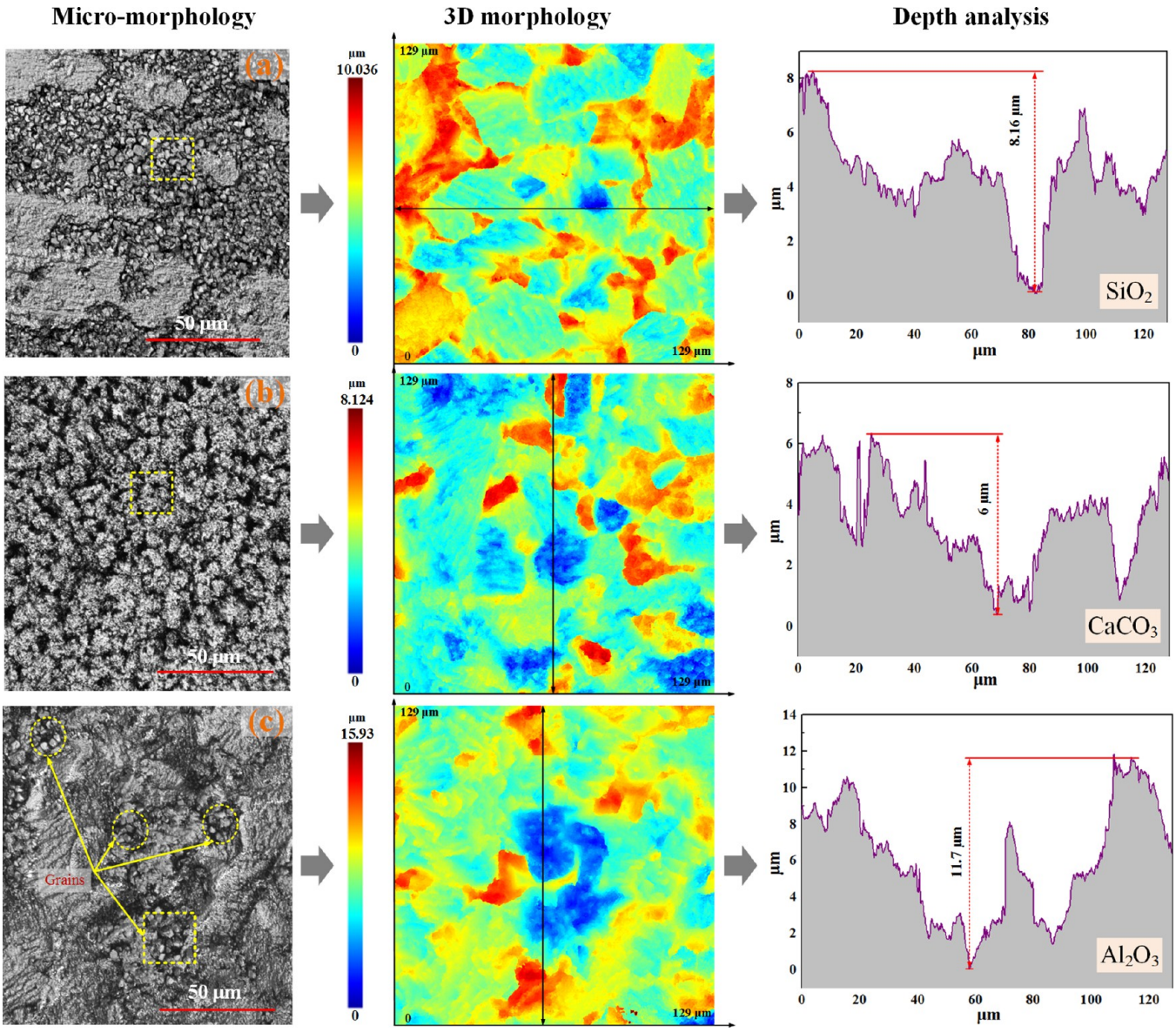

Figure 12. Morphologies of the deposit-covered steel area, the 3D morphology after the removal of the corrosion product, and the depth analysis of the corresponding area: (a) SiO_2, (b) $CaCO_3$, and (c) Al_2O_3.

$$Fe^{2+} + CO_3^{2-} \rightarrow FeCO_3 \quad (11)$$

$$Fe^{2+} + HCO_3^{-} \rightarrow FeCO_3 + H^+ \quad (12)$$

$$Fe^{2+} + H_2CO_3 \rightarrow FeCO_3 + 2H^+ \quad (13)$$

The formation of $FeCO_3$ depends on the local concentration of ions and pH.[47] At low pH, Fe^{2+} tends to form an amorphous $FeCO_3$ layer with nonprotective properties when the temperature is below 50 °C. At high pH, nucleation of $FeCO_3$ crystals could happen, as shown in Figure 12.

The pH measurement results show that the pH beneath all three types of deposits has increased. There are three possible explanations for this phenomenon. First, the deposits would be reacted with H^+ in the solution, leading to a reduction in the concentration of H^+.[23,40] Second, the deposits may obstruct the transfer of ions in the solution, resulting in the depleted hydrogen ions not being replenished in time.[12,39] Finally, a conjecture suggests that the dissolved carbon dioxide in solution may be more readily adsorbed onto the deposits compared to the carbon steel surface.[48−50] As a result, the solution beneath the deposits would have lower levels of carbon dioxide, resulting in a decrease in H^+ and an increased pH compared to those of the bare steel surface.

It is reported that the increase in pH would result in decreased corrosion rates.[12,46] This could explain the increase in the corrosion rate of the electrode covered with a deposit as the immersion time increased. However, the pH of the SiO_2-covered electrode shows no obvious changes. Therefore, there is another reason: at the beginning of the test, the hydrogen bubble that results from the reaction sticks to the electrode surface due to the deposits' obstructive effect.[30] This affects the electrode's actual area involved in the reaction, consequently influencing the obtained results.

According to reports, the potential of hydrogen reduction would decrease with the increase of solution pH in the iron-water system,[51,52] as shown in Figure 15. Therefore, the corrosion progress of electrodes covered by different deposits

https://doi.org/10.1021/acsomega.3c06189
ACS Omega 2023, 8, 44013−44029

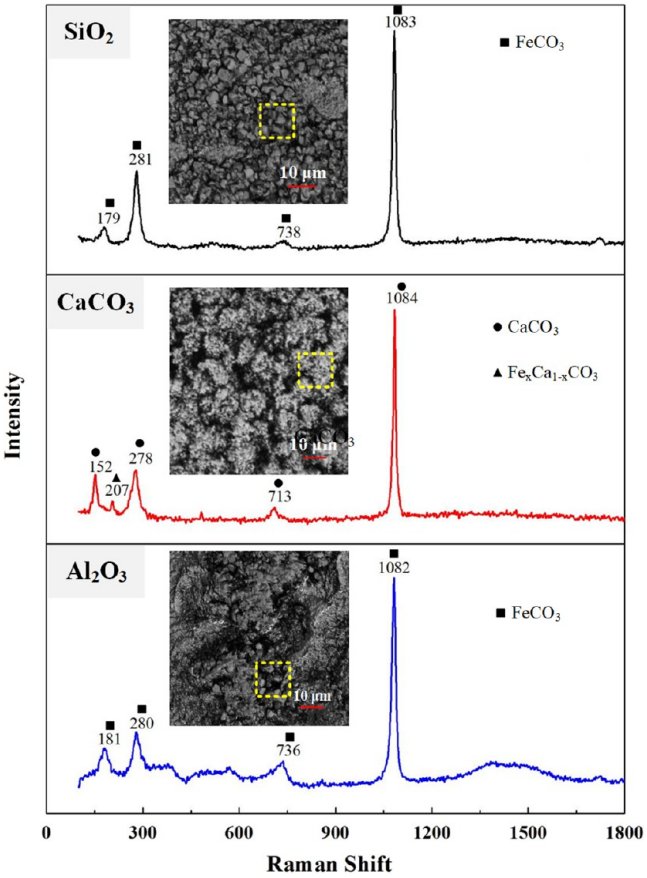

Figure 13. Raman results of the corrosion product from the selected area in Figure 12.

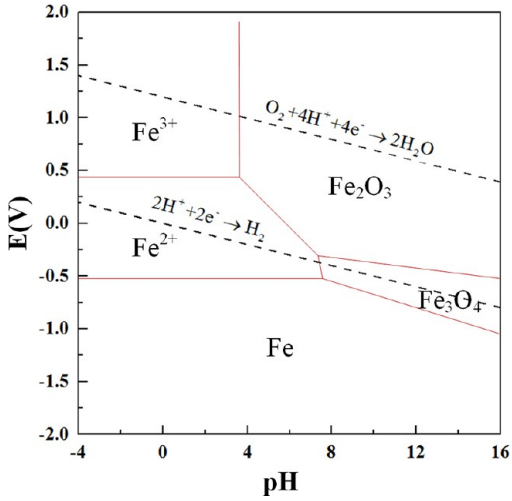

Figure 15. E-pH diagram for the iron-water system.

could be generally understood in accordance with the WBE test and electrochemical measurements, and the schematic diagram is plotted in Figure 16. As for the electrode covered by SiO_2 particles (Figure 16a), it acted as the cathode throughout the test. It might be because blocking plays a major role in the low porosity SiO_2 particles,[53] compared to the effect of pH variation. Moreover, a localized $FeCO_3$ layer would form beneath the silica particles, caused by the accumulation of Fe^{2+} and CO_3^{2-}. It might keep the corrosion inhibited in this area. However, the presence of gaps between the $FeCO_3$ layer would present a potential risk, leading to the formation of pits. The uneven distribution of $FeCO_3$ coverage might exacerbate the corrosion inhomogeneity of carbon steel on the SiO_2-covered area. At the beginning of the test, the pH beneath the $CaCO_3$ powder and Al_2O_3 particles was

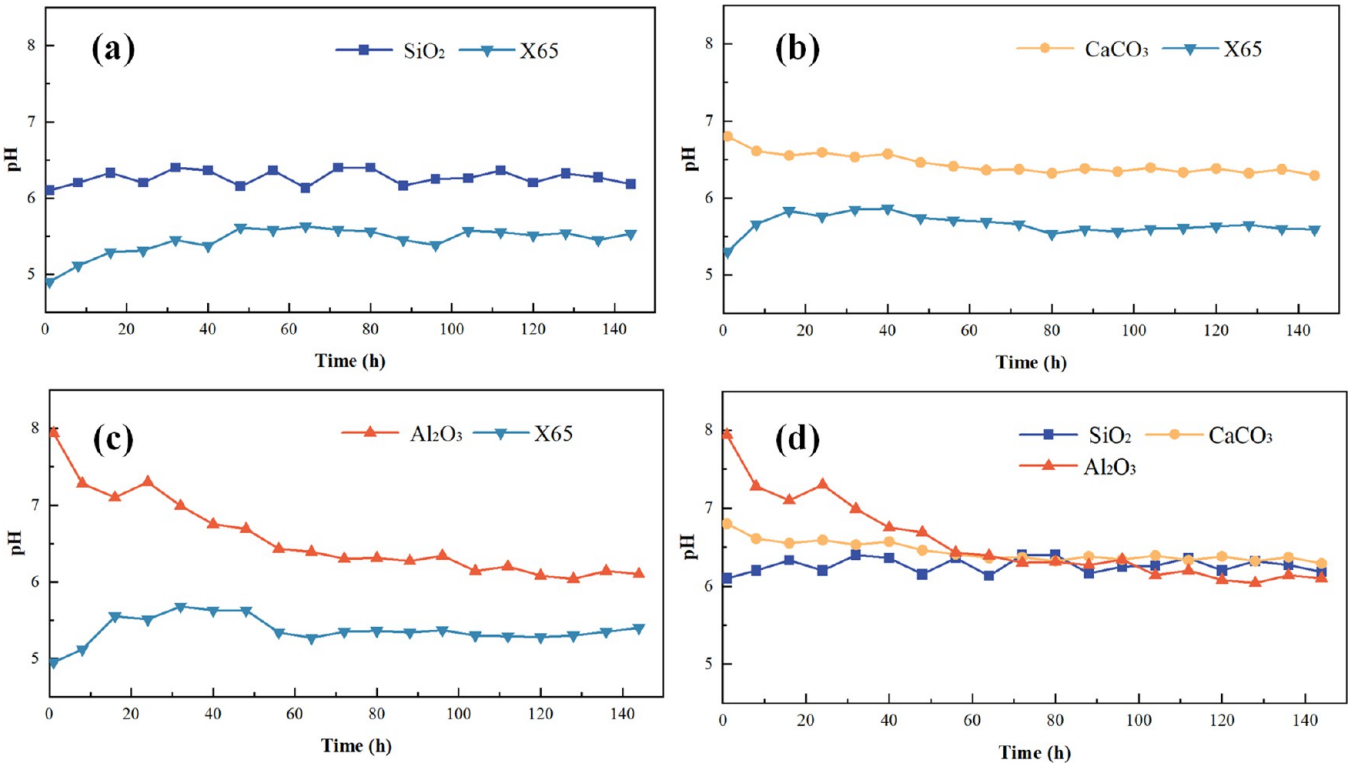

Figure 14. pH on the steel surface with and without deposits: (a) SiO_2, (b) $CaCO_3$, (c) Al_2O_3, and (d) difference of three deposits.

https://doi.org/10.1021/acsomega.3c06189
ACS Omega 2023, 8, 44013−44029

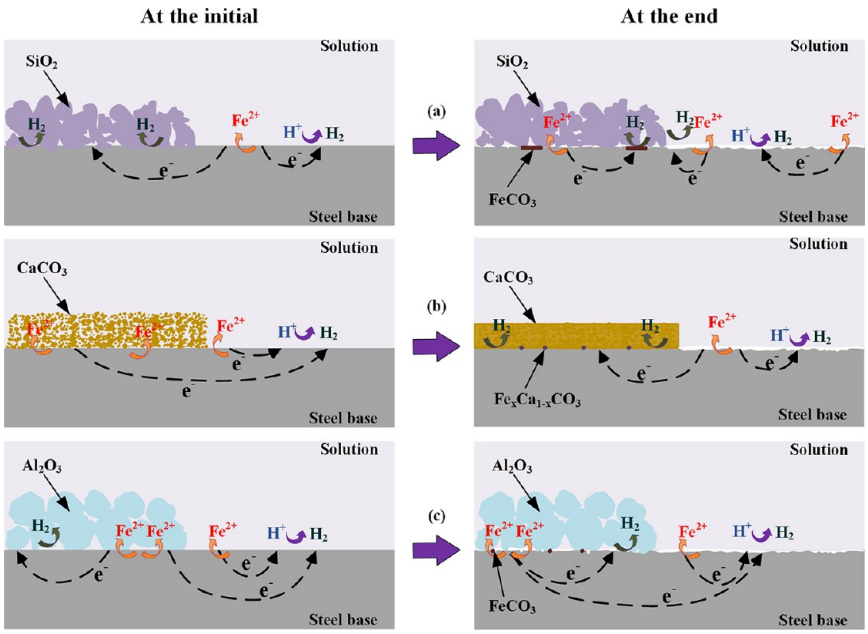

Figure 16. Schematic diagram of the nonuniform corrosion on the steel surface partly covered by a deposit: (a) SiO_2, (b) $CaCO_3$, and (c) Al_2O_3.

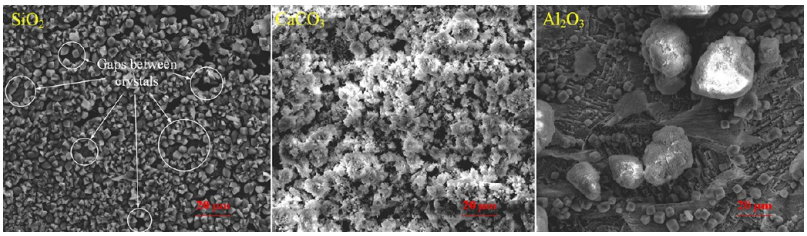

Figure A1. SEM images of the coupon steel on deposit-covered area (SiO_2, $CaCO_3$, and Al_2O_3) after the addition immersion test.

significantly higher than that of the bare steel, as shown in Figure 15. The corrosion potential of the deposit-covered ($CaCO_3$ and Al_2O_3) electrode would have a negative shift compared with that of the bare steel electrode. Once coupled to the bare steel electrode, the electrode covered by the deposit ($CaCO_3$ and Al_2O_3) would act as the anode due to the potential difference, as shown in Figure 16b,c. Along with the test, the reaction between alumina and the solution reached an equilibrium. The pH beneath the Al_2O_3 particles decreased gradually and stabilized, which was still higher than that of the bare steel. As a result, although the potential difference between the Al_2O_3-covered steel and the bare steel was smaller, the deposit-covered steel would always behave as the anode with a more negative corrosion potential. However, the $CaCO_3$ powder would aggregate on the surface of carbon steel and become viscous during the experiment.[54−56] The aggregation $CaCO_3$ would adsorb on the carbon steel surface,[54,57] and its blocking effect for the ions would also be enhanced. Compared to the effect of pH variation, the hindrance of $CaCO_3$ might play a major role in the corrosion process, resulting in a slightly positive increase in the corrosion potential. Thus, the area covered by $CaCO_3$ would change into a cathode gradually, as shown in Figure 16b. In summary, the corrosion initiation and propagation varied depending on the characteristics of the deposit as the corrosion proceeds.

Undoubtedly, small pits occurred under the deposits, due to the nonuniformity distribution of ions. These pits can increase the potential hazard of pipelines despite their shallow and small size. It indicates that there would be a tendency for the formation of penetrating pits beneath deposits.

5. CONCLUSIONS

- The presence of deposits reduced the corrosion rates of carbon steel, which is associated with the obstruction caused by deposits and the reduction in the mass transfer of chemical species.
- In the CO_2-containing brine solution with a low pH, the extent of corrosion varied depending on the deposit characteristics. The Al_2O_3-covered steel acted as the main anode with more negative potential when coupled with the bare steel. Similarly, the $CaCO_3$-covered steel acted as the anode with more negative potential initially. However, it gradually became the cathode as $CaCO_3$ aggregated during the experiment. The SiO_2-covered steel acted as the cathode with more positive potential, and the localized $FeCO_3$ layer formed beneath the SiO_2 mineral.
- Pits were found beneath the deposits, which were shallow and small. The pitting depth was in sequence Al_2O_3 > SiO_2 > $CaCO_3$.
- WBE could provide the spatial and temporal information of under deposit corrosion by measuring the corrosion potential and macro-cell current distribution, and then the initiation and propagation of under deposit corrosion were effectively reflected.

https://doi.org/10.1021/acsomega.3c06189
ACS Omega 2023, 8, 44013−44029

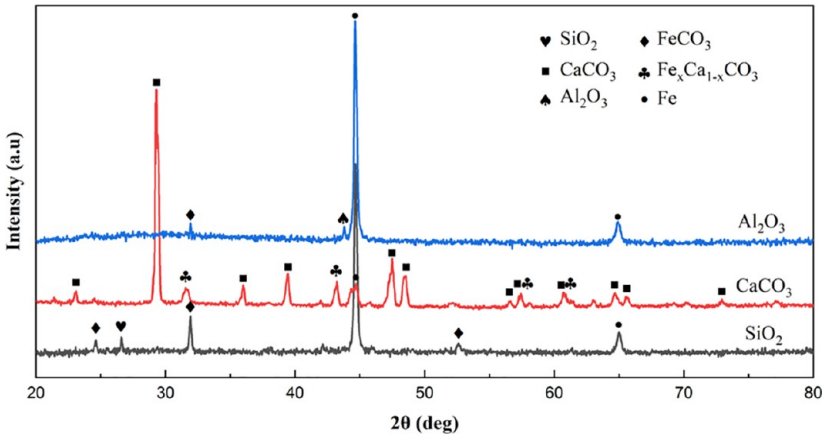

Figure A2. XRD characterization results of corrosion products on the steel coupon beneath three deposits in the addition immersion test.

■ APPENDIX

The morphologies of the coupon steel on the deposit-covered area (SiO_2, $CaCO_3$, and Al_2O_3) in the addition immersion test are shown in Figure A1. The corrosion products identified by XRD after the addition immersion test are shown in Figure A2.

■ AUTHOR INFORMATION

Corresponding Author

Yunze Xu − *School of Naval Architecture and Ocean Engineering and State Key Laboratory of Structural Analysis for Industrial Equipment, Dalian University of Technology, Dalian 116024, China*; Email: xuyunze123@163.com

Authors

Limin He − *School of Naval Architecture and Ocean Engineering, Dalian University of Technology, Dalian 116024, China*; orcid.org/0000-0002-8002-1367

Yihan Wang − *School of Naval Architecture and Ocean Engineering, Dalian University of Technology, Dalian 116024, China*

Qiliang Zhang − *School of Naval Architecture and Ocean Engineering, Dalian University of Technology, Dalian 116024, China*

XinCheng Li − *School of Naval Architecture and Ocean Engineering, Dalian University of Technology, Dalian 116024, China*

Yi Huang − *School of Naval Architecture and Ocean Engineering and State Key Laboratory of Structural Analysis for Industrial Equipment, Dalian University of Technology, Dalian 116024, China*

Complete contact information is available at: https://pubs.acs.org/10.1021/acsomega.3c06189

Notes

The authors declare no competing financial interest.

■ ACKNOWLEDGMENTS

This research was sponsored by the National Key R&D Program of China (No. 2022YFC2806200) and the Natural Science Foundation of China (No. 52001055).

■ REFERENCES

(1) Osorio-Celestino, G. R.; Hernandez, M.; Solis-Ibarra, D.; Tehuacanero-Cuapa, S.; Rodríguez-Gómez, A.; Gómora-Figueroa, A. P. Influence of Calcium Scaling on Corrosion Behavior of Steel and Aluminum Alloys. *ACS Omega* **2020**, *5*, 17304−17313.

(2) Sliem, M. H.; Fayyad, E. M.; Abdullah, A. M.; Younan, N. A.; Al-Qahtani, N.; Nabhan, F. F.; Ramesh, A.; Laycock, N.; Ryan, M. P.; Maqbool, M.; et al. Monitoring of under deposit corrosion for the oil and gas industry: A review. *J. Pet. Sci. Eng.* **2021**, *204*, No. 108752.

(3) Brown, B.; Moloney, J. *In Under-deposit corrosion*; Woodhead Publishing Series in Energy: United States, 2017.

(4) Pang, L.; Wang, Z.; Emori, W.; Zheng, Y. Under-Deposit Corrosion of Carbon Steel Beneath Full Coverage of $CaCO_3$ Deposit Layer under Different Atmospheres. *J. Mater. Eng. Perform.* **2021**, *30*, 7552−7563.

(5) Wang, X.; Melchers, R. E. Corrosion of carbon steel in presence of mixed deposits under stagnant seawater conditions. *J. Loss Prev. Process Ind.* **2017**, *45*, 29−42.

(6) Mahidashti, Z.; Rezaei, M.; Asfia, M. P. Internal under-deposit corrosion of X60 pipeline steel upon installation in a chloride-containing soil environment. *Colloids Surf., A* **2020**, *602*, No. 125120.

(7) Wang, X.; Melchers, R. E. Long-term under-deposit pitting corrosion of carbon steel pipes. *Ocean Eng.* **2017**, *133*, 231−243.

(8) He, L.; Xu, Y.; Wang, X.; Huang, Y. Understanding the propagation of non-uniform corrosion on a steel surface covered by marine sand. *Corrosion* **2019**, *75*, 1487−1501.

(9) Huang, Y.; Xu, Y.; Li, B.; Ying, L.; Yang, F.; Wang, X. Novel electrical resistance method to measure underdeposit corrosion and its inhibition in pipeline steels. *Corros. Eng., Sci. Technol.* **2016**, *51*, 211−222.

(10) Xu, Y. Z.; Zhu, Y. S.; Liu, L.; He, L. M.; Wang, X. N.; Huang, Y. The study of the localized corrosion caused by mineral deposit using novel designed multi-electrode sensor system. *Mater. Corros.* **2017**, *68*, 632−644.

(11) Yang, R.; Xu, P.; Xin, G. Influence of Silica Particle Size on the Corrosion Behavior of Electroplated Silica−Ni Hybrid Layer. *ACS Omega* **2020**, *5*, 15983−15991.

(12) Huang, J. Mechanistic Study of Under Deposit Corrosion of Mild Steel in Aqueous Carbon Dioxide Solution. PhD, **2013**.

(13) Xu, Y.; Huang, Y.; He, L.; Yang, F.; Wang, X. Experimental study on under-deposit corrosion and its inhibition using electrochemical methods and electronic coupon technique. *Anti-Corros. Methods Mater.* **2017**, *64*, 148−161.

(14) Xu, Y. Z.; Yang, L. J.; He, L. M.; Huang, Y.; Wang, X. N. The monitoring of galvanic corrosion behaviour caused by mineral deposit in pipeline working conditions using ring form electronic resistance sensor system. *Corros. Eng., Sci. Technol.* **2016**, *51*, 606−620.

(15) Wu, Y.; Zhang, D.; Cai, G.; Zhang, X.; Dong, Z. Effects of temperature on polarity reversal of under deposit corrosion of mild steel in oilfield produced water. *Corros. Eng., Sci. Technol.* **2020**, *55*, 708−720.

(16) Xiong, Q.; Hu, J.; Gu, C.; Feng, M.; Zhang, Z.; Zhong, X. The study of under deposit corrosion of carbon steel in the flowback water during shale gas production. *Appl. Surf. Sci.* **2020**, *523*, No. 146534.
(17) Li, Y. Z.; Xu, N.; Guo, X. P.; Zhang, G. A. The role of acetic acid or H^+ in initiating crevice corrosion of N80 carbon steel in CO_2-saturated NaCl solution. *Corros. Sci.* **2017**, *128*, 9−22.
(18) Wang, Z.; Wang, Y.; Wang, C. Area Ratio of Cathode/Anode Effect on the Galvanic Corrosion of High Potential Difference Coupling in Seawater. *IOP Conf. Ser.: Mater. Sci. Eng.* **2018**, *322*, No. 022046, DOI: 10.1088/1757-899X/322/2/022046.
(19) Tan, Y.; Fwu, Y.; Bhardwaj, K. Electrochemical evaluation of under-deposit corrosion and its inhibition using the wire beam electrode method. *Corros. Sci.* **2011**, *53*, 1254−1261.
(20) Zhang, G. A.; Yu, N.; Yang, L. Y.; Guo, X. P. Galvanic corrosion behavior of deposit-covered and uncovered carbon steel. *Corros. Sci.* **2014**, *86*, 202−212.
(21) Suarez, E. M.; Lepková, K.; Forsyth, M.; Tan, M. Y.; Kinsella, B.; Machuca, L. L. In Situ Investigation of Under-Deposit Microbial Corrosion and its Inhibition Using a Multi-Electrode Array System. *Front. Bioeng. Biotechnol.* **2022**, *9*, No. 803610.
(22) Liu, H.; Meng, G.; Li, W.; Gu, T.; Liu, H. Microbiologically Influenced Corrosion of Carbon Steel Beneath a Deposit in CO_2-Saturated Formation Water Containing Desulfotomaculum nigrificans. *Front. Microbiol.* **2019**, *10*, No. 03082.
(23) Suarez, E. M.; Machuca, L. L.; Kinsella, B.; Lepková, K. CO_2 Corrosion Inhibitors Performance at Deposit-Covered Carbon Steel and Their Adsorption on Different Deposits. *Corrosion* **2019**, *75*, 1118−1127.
(24) Vedapriya, P. Investigation of inhibition processes at sand-deposited surfaces. PhD, **2013**.
(25) Jeannin, M.; Calonnec, D.; Sabot, R.; Refait, P. Role of a clay sediment deposit on the corrosion of carbon steel in 0.5mol/L NaCl solutions. *Corros. Sci.* **2010**, *52*, 2026−2034.
(26) McCafferty, E.; Hackerman, N. Kinetics of Iron Corrosion in Concentrated Acidic Chloride Solutions. *J. Electrochem.* **1972**, *119*, 999−1009.
(27) Tan, Z.; Yang, L.; Zhang, D.; Wang, Z.; Cheng, F.; Zhang, M.; Jin, Y. Development mechanism of internal local corrosion of X80 pipeline steel. *J. Mater. Sci. Technol.* **2020**, *49*, 186−201.
(28) Zhang, G. A.; Cheng, Y. F. On the fundamentals of electrochemical corrosion of X65 steel in CO_2-containing formation water in the presence of acetic acid in petroleum production. *Corros. Sci.* **2009**, *51*, 87−94.
(29) Xu, Y.; Liu, L.; Xu, C.; Wang, X.; Tan, M. Y.; Huang, Y. Electrochemical characteristics of the dynamic progression of erosion-corrosion under different flow conditions and their effects on corrosion rate calculation. *J. Solid State Electrochem.* **2020**, *24*, 2511−2524.
(30) Zeng, Z.; Lillard, R. S.; Cong, H. Effect of Salt Concentration on the Corrosion Behavior of Carbon Steel in CO_2 Environment. *Corrosion* **2016**, *72*, 805−823.
(31) Almeida, T. C.; Bandeira, M. C. E.; Moreira, R. M.; Mattos, O. R. Discussion on "Electrochemistry of CO_2 corrosion of mild steel: Effect of CO_2 on iron dissolution reaction" by A. Kahyarian, B. Brown, S. Nesic, [Corros. Sci. 129 (2017) 146−151]. *Corros. Sci.* **2018**, *133*, 417−422.
(32) Kahyarian, A.; Brown, B.; Nesic, S. Electrochemistry of CO_2 corrosion of mild steel: Effect of CO_2 on iron dissolution reaction. *Corros. Sci.* **2017**, *129*, 146−151.
(33) Bockris, J. O.; Drazic, D.; Despic, A. R. The ElectrodeE Kinetics of the Deposition and Dissolution of Iron. *Electrochim. Acta* **1961**, *4*, 325−361.
(34) Li, R.; Huang, H.; Wang, X.; Wang, Y. Effect of ammonium salt on corrosion of pipelines and components in a crude oil distillation column: Electrochemical and AIMD studies. *Corros. Sci.* **2022**, *203*, No. 110362.
(35) Du, P.; Deng, S.; Du, G.; Shao, D.; Xu, D.; Li, X. Synergistic inhibition effect of Mikania micrantha extract with potassium iodide on the corrosion of cold rolled steel in methanesulfonic acid solution. *Corros. Sci.* **2023**, *220*, No. 111296.
(36) Dufresne, W. J. B.; Rufledt, C. J.; Marshall, C. P. Raman spectroscopy of the eight natural carbonate minerals of calcite structure. *J. Raman Spectrosc.* **2018**, *49*, 1999−2007.
(37) Tavares, L. M.; Costa, E. M. D.; Andrade, J. J. D. O.; Hubler, R.; Huet, B. Effect of calcium carbonate on low carbon steel corrosion behavior in saline CO_2 high pressure environments. *Appl. Surf. Sci.* **2015**, *359*, 143−152.
(38) Shatskiy, A.; Borzdov, Y. M.; Litasov, K. D.; Kupriyanov, I. N.; Ohtani, E.; Palyanov, Y. N. Phase relations in the system $FeCO_3$-$CaCO_3$ at 6 GPa and 900−1700 C and its relation to the system $CaCO_3$-$FeCO_3$-$MgCO_3$. *Am. Mineral.* **2014**, *99*, 773−785.
(39) Iwai, M.; Kikuchi, T. Chemical stability of porous anodic aluminum oxide in both acidic and alkaline solutions. *Thin Solid Films* **2023**, *771*, No. 139784.
(40) Boukerche, I.; Djerad, S.; Benmansour, L.; Tifouti, L.; Saleh, K. Degradability of aluminum in acidic and alkaline solutions. *Corros. Sci.* **2014**, *78*, 343−352.
(41) Farelas, F.; Galicia, M.; Brown, B.; Nesic, S.; Castaneda, H. Evolution of dissolution processes at the interface of carbon steel corroding in a CO_2 environment studied by EIS. *Corros. Sci.* **2010**, *52*, 509−517.
(42) Eliyan, F. F.; Alfantazi, A. On the theory of CO_2 corrosion reactions-Investigating their interrelation with the corrosion products and API-X100 steel microstructure. *Corros. Sci.* **2014**, *85*, 380−393.
(43) Li, P.; Tan, T. C.; Lee, J. Y. Impedance Spectra of the Anodic Dissolution of Mild Steel in Sulfuric Acid. *Corros. Sci.* **1996**, *38*, 1935−1955.
(44) Kahyarian, A.; Nesic, S. A New Narrative for CO_2 Corrosion of Mild Steel. *J. Electrochem. Soc.* **2019**, *166*, C3048−C3063.
(45) Remita, E.; Tribollet, B.; Sutter, E.; Vivier, V.; Ropital, F.; Kittel, J. Hydrogen evolution in aqueous solutions containing dissolved CO_2: Quantitative contribution of the buffering effect. *Corros. Sci.* **2008**, *50*, 1433−1440.
(46) De Motte, R.; Mingant, R.; Kittel, J.; Ropital, F.; Combrade, P.; Necib, S.; Deydier, V.; Crusset, D. Near surface pH measurements in aqueous CO_2 corrosion. *Electrochim. Acta* **2018**, *290*, 605−615.
(47) Sk, M. H.; Abdullah, A. M.; Ko, M.; Ingham, B.; Laycock, N.; Arul, R.; Williams, D. E. Local supersaturation and the growth of protective scales during CO_2 corrosion of steel: Effect of pH and solution flow. *Corros. Sci.* **2017**, *126*, 26−36.
(48) Li, R.; Zhang, Y.; Li, M.; Wang, Y. Adsorption behaviors of NH_3 and HCl molecules on Fe-based crystal planes: A DFT study. *Chem. Eng. Sci.* **2021**, *246*, No. 116976.
(49) Hou, B. S.; Zhang, Q. H.; Li, Y. Y.; Zhu, G. Y.; Zhang, G. A. Influence of corrosion products on the inhibition effect of pyrimidine derivative for the corrosion of carbon steel under supercritical CO_2 conditions. *Corros. Sci.* **2020**, *166*, No. 108442.
(50) Wang, H.; Nie, X.; Chen, Y.; Guo, X.; Song, C. Facet effect on CO_2 adsorption, dissociation and hydrogenation over Fe catalysts: Insight from DFT. *J. CO2 Util.* **2018**, *26*, 160−170.
(51) Kim, Y.; Kim, J. Improvement of corrosion resistance for low carbon steel pipeline in district heating environment using transient oxygen injection method. *J. Ind. Eng. Chem.* **2019**, *70*, 169−177.
(52) Lazzari, L.; Pedeferri, M. *Corrosion Science and Engineering*; Springer Nature Switzerland AG: Gewerbestrasse 11, 6330 Cham, Switzerland, 2018.
(53) Cao, C. *Principles of Electrochemistry of Corrosion*; Chemical Industry Press: Beijing, China, 2008.
(54) Shi, J. Dispersion and Encapsulation of Nanometer Caleium Carbonate with Polymer. PhD, **2005**.
(55) Cai, H.; Li, S.; Tian, G.; Wang, H.; Wang, J. Reinforcement of natural rubber latex film by ultrafine calcium carbonate. *J. Appl. Polym. Sci.* **2003**, *87*, 982−985.
(56) Wang, Q.; Wang, T.; Sun, X.; Huang, C.; Yan, Y.; Kangying. Research of Viscosity of Calcium Carbonate Filled Polypropylene in Dynamic Extrusion. *Recent Pat. Mater. Sci.* **2014**, *7*, 60−63.
(57) Wang, Q.; Peng, J.; Zhou, L.; Tang, T.; Li, S.; Chen, H.; Wang, H.; Zheng, G.; Yang, X.; Qian, L. Influence of surface property of

$CaCO_3$ fillers on apparent viscosity of filled polydimethylsiloxane. *Colloids Surf., A* **2021**, *626*, No. 127044.

https://doi.org/10.1021/acsomega.3c06189
ACS Omega 2023, 8, 44013−44029